Testing viscoelastic numerical schemes using the Oldroyd-B fluid in Newtonian kinematics

J.D. Evans*
Department of Mathematical Sciences, University of Bath,
Bath, BA2 7AY, United Kingdom

H.L. França†
I.L. Palhares Junior‡
C.M. Oishi§
Departamento de Matematica, Estatistica e Computação, Universidade Estadual Paulista,
Presidente Prudente, Brazil

January 14, 2020

Abstract

We focus here on using a Newtonian velocity field to evaluate numerical schemes for two different formulations of viscoelastic flow. The two distinct formulations we consider, correspond to either using a fixed basis for the elastic stress or one that uses the flow directions or streamlines. The former is the traditional Cartesian stress formulation, whilst the later may be referred to as the natural stress formulation of the equations. We choose the Oldroyd-B fluid and three benchmarks in computational rheology: the 4:1 contraction flow, the stick-slip and cross-slot problems. In the context of the contraction flow, fixing the kinematics as Newtonian, actually gives a larger stress singularity at the re-entrant corner, the matched asymptotics of which are presented here. Numerical results for temporal and spatial convergence of the two formulations are compared first in this decoupled velocity and elastic stress situation, to assess the performance of the two approaches. This may be regarded as an intermediate test case before proceeding to the far more difficult fully coupled velocity and stress situation. We also present comparison results between numerics and asymptotics for the stick-slip problem. Finally, the natural stress formulation is used to investigate the cross-slot problem, again in a Newtonian velocity field.

Keywords: matched asymptotics, stress singularity, boundary layers, Oldroyd-B fluid, numerical verification

* e-mail: masjde@bath.ac.uk, Phone: +44 1225 386994, Fax: +44 1225 386492
† e-mail: franca.hugo1@gmail.com
‡ e-mail: irineulopespalhares@gmail.com
§ e-mail: cassio.oishi@unesp.br, Phone: +55 18 32295623

1 Introduction

Advances in numerical methodologies have contributed to the investigation into the rheological response behaviour of complex materials in specific geometries. These include contraction type flows [2] or new micro-devices such as cross-slot flows [3]. These flow geometries are used in general to measure the extensional properties and explore fluid rheology responses, where quite distinct behaviour from Newtonian fluids are obtained for viscoelastic fluids such as Boger fluids [12].

In recent decades, since the publication of Walters and Webster [4] evidencing the challenges involved in the contraction geometry and its admission as a classical benchmark problem back in 1988 [5], it has been widely used for validation/verification of numerical codes. In particular, not only the accuracy [6]–[11] but also the stability of the numerical methodologies [12]–[15] have been exhaustively verified. Besides, in-house code validations, this benchmark problem has been also applied for verifying open-source solvers provided in the literature, as for example, in the implementation of toolboxes in OpenFOAM [16, 17, 18]. One aspect of the many code verifications described in the literature for contraction flows, is their predominant focus upon vortex behaviour and pressure drops. Attention is only given briefly to the asymptotic behaviour of the stress in the vicinity of the sharp re-entrant corner [7, 8, 19], despite the presence of sharp stress wall boundary layers which have not been investigated. Thus, in order to present further knowledge about the stress singularity and to allow for continuous improvement of the codes, in this work we have adopted Newtonian kinematics. This allows for a careful comparison to be made between the asymptotics and numerical computations in a simplified, intermediate case. Imposing a Newtonian velocity field, we propose to use it as a simplified benchmark for testing viscoelastic numerical schemes focusing on the behaviour of the stress components around corners.

An additional complex benchmark problem [5] for testing viscoelastic numerical methods is the stick-slip flow [20, 36]. In this type of flow, the main difficulty is to understand the behaviour at the die exit where a stress singularity is present due to the change in boundary conditions from no-slip inside the die to slip along the free surface outside of the die. The stick-slip problem is a simplified case of the die-swell problem [38] which is a benchmark problem for moving boundary and free surface codes [21]. Again we use the Newtonian kinematics for solving the stick-slip problem in order to gain more insights on the boundary layers and stress singularities in a complex geometry relevant to polymer processing applications. In a Newtonian velocity field, the behaviour of the Oldroyd-B fluid for the stick-slip singularity has been classified in [36], where it is was shown that the stress singularity is transmitted along the free-surface. We support these results here with numerical simulations confirming such theoretical conclusions.

The studies concerning the benchmark flows will be done for two distinct mathematical methodologies: the Cartesian and the natural stress formulations. The former, is widely applied in the computational rheology, whilst the latter has been recently applied for unsteady viscoelastic simulations [37]. Using the intermediate case of a Newtonian velocity field, allows a direct comparison to be made between the two formulations for numerical schemes, since the results can be benchmarked to the known asymptotics around singular points for contraction and stick-slip flows. As yet, the singularity for Oldroyd-B in stick-slip flow has not been classified for the true viscoelastic velocity field and is an outstanding problem. Not only do these problems allow spatial convergence between the formulations to be analysed but also the temporal convergence of the schemes.

It is worth noting that the assumption of fixed Newtonian kinematics for Oldroyd-B fluids has previously been applied for asymptotic and computational studies of other benchmark problems, for instance, the flow of a viscoelastic fluid around a cylinder [22, 23]. It has also been used in early numerical work for the stick-slip problem [24, 25], before the asymptotic classification of the problem. Further, for other viscoelastic models, such as Phan-Thien–Tanner (PTT) [26, 27] and Giesekus [28], a Newtonian velocity field predominates at stress singularities for sharp corners [29, 30, 31] and stick-slip [32, 33]. As such, using a Newtonian velocity field for such models is then wholly relevant and evaluating how the Oldroyd-B model behaves provides a useful comparison [36].

The layout of the paper is as follows. In section 2 we present the governing equations and formulations of the Cartesian and natural stress statements. Section 3 derives the stress singularity at sharp corners for Oldroyd-B in Newtonian kinematics using the method of matched asymptotic expansions. This completes

the preliminary streamline analysis of Renardy [41] for this situation and the derived behaviours verified through direct numerical integration of the equations along the analytical streamlines. These asymptotic results are then used in section 4 to investigate the spatial convergence of the numerical schemes at the 270^o corner for the 4:1 contraction. Temporal and global convergence results are also presented. The stick-slip problem is then considered in section 5. In section 6, the cross slot flow is investigated numerically for the behaviour of the natural stress variables close to the stagnation region.

2 Mathematical model

The non-dimensional governing equations for isothermal incompressible flow, are the continuity and momentum equations

$$\nabla \cdot \mathbf{v} = 0, \tag{2.1}$$

$$\mathrm{Re}\left(\frac{\partial \mathbf{v}}{\partial t} + \mathbf{v}\cdot\nabla\mathbf{v}\right) = -\nabla p + \beta\nabla^2\mathbf{v} + \gamma\nabla\cdot\mathbf{T}^p, \tag{2.2}$$

where $\mathbf{v}$ and p are the velocity and pressure fields, respectively, while Re is the Reynolds number and $\beta \in [0,1]$ is the viscosity ratio or dimensionless solvent viscosity. In Eq. (2.2), the parameter γ is only adopted for representing the following situations:

$$\gamma = \begin{cases} 0, & \text{Newtonian velocity field,} \\ 1, & \text{Viscoelastic velocity field.} \end{cases} \tag{2.3}$$

It is worth to notice that for the asymptotic stress analysis, a typical assumption is that the velocity field around the singularity is Newtonian ($\gamma = 0$) allowing the integration of the governing equation along the streamlines, as was done for example in [36]. However, if the interest is only from the numerical point-of-view, then the complete system of equations is used with no assumption on the velocity field, i.e., $\gamma = 1$ in Eq. (2.2).

For viscoelastic fluids, the term $\mathbf{T}^p$ in Eq. (2.2) represents the non-Newtonian contribution in the flow which is generally modelled by a hyperbolic constitutive equation. In particular, if the Oldroyd-B model is adopted, the constitutive equation is

$$\mathbf{T}^p + \mathrm{Wi}\ \overset{\triangledown}{\mathbf{T}}{}^p = 2(1-\beta)\mathbf{D}, \tag{2.4}$$

where $\mathbf{D} = \frac{1}{2}(\nabla\mathbf{v} + (\nabla\mathbf{v})^T)$ is the rate-of-strain tensor and $\overset{\triangledown}{\mathbf{T}}{}^p$ the upper-convected derivative of the polymer extra-stress. In Eq. (2.4), Wi represents the Weissenberg number which is used to measure the elasticity or memory of the fluid.

The most common formulation used to construct the component equations for the constitutive equation (2.4) is based upon the Cartesian decomposition of the tensor $\mathbf{T}^p$, i.e.

$$\mathbf{T}^p = T^p_{11}\mathbf{i}\mathbf{i}^T + T^p_{12}\left(\mathbf{i}\mathbf{j}^T + \mathbf{j}\mathbf{i}^T\right) + T^p_{22}\mathbf{j}\mathbf{j}^T, \tag{2.5}$$

where $\mathbf{i}$ and $\mathbf{j}$ are unit vectors in fixed Cartesian x and y directions. In this framework, the component form of the polymer constitutive equation (2.4) for the Cartesian polymer extra-stresses $T^p_{11}, T^p_{12}, T^p_{22}$ is

$$T^p_{11} + \mathrm{Wi}\left(\frac{T^p_{11}}{\partial t} + u\frac{\partial T^p_{11}}{\partial x} + v\frac{\partial T^p_{11}}{\partial y} - 2\frac{\partial u}{\partial x}T^p_{11} - 2\frac{\partial u}{\partial y}T^p_{12}\right) = 2(1-\beta)\frac{\partial u}{\partial x}, \tag{2.6}$$

$$T^p_{22} + \mathrm{Wi}\left(\frac{\partial T^p_{22}}{\partial t} + u\frac{\partial T^p_{22}}{\partial x} + v\frac{\partial T^p_{22}}{\partial y} - 2\frac{\partial v}{\partial y}T^p_{22} - 2\frac{\partial v}{\partial x}T^p_{12}\right) = 2(1-\beta)\frac{\partial v}{\partial y}, \tag{2.7}$$

$$T^p_{12} + \mathrm{Wi}\left(\frac{\partial T^p_{12}}{\partial t} + u\frac{\partial T^p_{12}}{\partial x} + v\frac{\partial T^p_{12}}{\partial y} - \frac{\partial v}{\partial x}T^p_{11} - \frac{\partial u}{\partial y}T^p_{22}\right) = (1-\beta)\left(\frac{\partial u}{\partial y} + \frac{\partial v}{\partial x}\right), \tag{2.8}$$

where the velocity field has components

$$\mathbf{v} = u\mathbf{i} + v\mathbf{j}. \tag{2.9}$$

In computational rheology this Cartesian stress formulation (CSF) is widely used by many authors to construct in-house codes [38, 12] and open free codes [17, 18].

An alternative formulation is to use the streamlines to construct the constitutive equations of the polymer extra-stresses as proposed by Renardy [39] and earlier researchers [40]. This natural stress formulation (NSF) uses the velocity field and a suitable orthogonal vector to span the polymer extra-stress field as follows

$$\mathbf{T}^p = \frac{(1-\beta)}{\mathrm{Wi}}\left(-\mathbf{I} + \lambda\mathbf{v}\mathbf{v}^T + \mu(\mathbf{v}\mathbf{w}^T + \mathbf{w}\mathbf{v}^T) + \nu\mathbf{w}\mathbf{w}^T\right), \tag{2.10}$$

with

$$\mathbf{w} = \frac{1}{|\mathbf{v}|^2}(-v\mathbf{i} + u\mathbf{j}).$$

In steady state, the natural stress variables λ, μ, ν satisfy the equations

$$\mathrm{Wi}\left((\mathbf{v}\cdot\nabla)\lambda + 2\mu\nabla\cdot\mathbf{w}\right) + \lambda = \frac{1}{|\mathbf{v}|^2}, \tag{2.11}$$

$$\mathrm{Wi}\left((\mathbf{v}\cdot\nabla)\mu + \nu\nabla\cdot\mathbf{w}\right) + \mu = 0, \tag{2.12}$$

$$\mathrm{Wi}(\mathbf{v}\cdot\nabla)\nu + \nu = |\mathbf{v}|^2, \tag{2.13}$$

whilst the transient formulation is more conveniently expressed through the scaled variables

$$\hat{\lambda} = |\mathbf{v}|^2\lambda, \qquad \hat{\mu} = \mu, \qquad \hat{\nu} = \frac{\nu}{|\mathbf{v}|^2}, \tag{2.14}$$

and take the form

$$\left[\frac{\partial\hat{\lambda}}{\partial t} + \frac{2\hat{\mu}}{|\mathbf{v}|^2}\left(v\frac{\partial u}{\partial t} - u\frac{\partial v}{\partial t}\right) + |\mathbf{v}|^2(\mathbf{v}\cdot\nabla)\left(\frac{\hat{\lambda}}{|\mathbf{v}|^2}\right) + 2\hat{\mu}|\mathbf{v}|^2\nabla\cdot\mathbf{w}\right] + \frac{1}{\mathrm{Wi}}\left(\hat{\lambda} - 1\right) = 0, \tag{2.15}$$

$$\left[\frac{\partial\hat{\mu}}{\partial t} + \left(\frac{\hat{\lambda}-\hat{\nu}}{|\mathbf{v}|^2}\right)\left(u\frac{\partial v}{\partial t} - v\frac{\partial u}{\partial t}\right) + (\mathbf{v}\cdot\nabla)\hat{\mu} + \hat{\nu}|\mathbf{v}|^2\nabla\cdot\mathbf{w}\right] + \frac{\hat{\mu}}{\mathrm{Wi}} = 0, \tag{2.16}$$

$$\left[\frac{\partial\hat{\nu}}{\partial t} + \frac{2\hat{\mu}}{|\mathbf{v}|^2}\left(u\frac{\partial v}{\partial t} - v\frac{\partial u}{\partial t}\right) + \frac{1}{|\mathbf{v}|^2}(\mathbf{v}\cdot\nabla)\left(\hat{\nu}|\mathbf{v}|^2\right)\right] + \frac{1}{\mathrm{Wi}}\left(\hat{\nu} - 1\right) = 0, \tag{2.17}$$

The variables $\hat{\lambda}, \hat{\mu}, \hat{\nu}$ may be interpreted as scaled conformation stress components aligned along streamlines. The normal conformation stress component in the direction of flow along a streamline is $\hat{\lambda}$, whilst the normal conformation stress component perpendicular to the streamline is $\hat{\nu}$ and $\hat{\mu}$ is the shear stress component. We will utilise both forms, with (2.11)–(2.13) being appropriate for the singularity analysis of section 3 and (2.15)–(2.17) for numerical implementation in section 4. The component stresses of the two formulations are linked by the expressions

$$\frac{\mathrm{Wi}}{(1-\beta)}T^p_{11} = -1 + \lambda u^2 - \mu\frac{2uv}{|\mathbf{v}|^2} + \nu\frac{v^2}{|\mathbf{v}|^4}, \tag{2.18}$$

$$\frac{\mathrm{Wi}}{(1-\beta)}T^p_{12} = \lambda uv + \mu\frac{(u^2-v^2)}{|\mathbf{v}|^2} - \nu\frac{uv}{|\mathbf{v}|^4}, \tag{2.19}$$

$$\frac{\mathrm{Wi}}{(1-\beta)}T^p_{22} = -1 + \lambda v^2 + \mu\frac{2uv}{|\mathbf{v}|^2} + \nu\frac{u^2}{|\mathbf{v}|^4}, \tag{2.20}$$

which follow directly from (2.10).

3 Singularity behaviour at sharp corners

Renardy [41] has given a preliminary analysis of the stress singularity at a re-entrant corner for the upper convected Maxwell model in fixed Newtonian kinematics. Here, we complete that analysis using the method of matched asymptotic expansions in section 3.1 and then verify it numerically in section 3.2. For the purposes of this section, we rewrite (2.2) in the form

$$0 = -\nabla p + \nabla \cdot \mathbf{T}, \tag{3.1}$$

where the extra-stress tensor $\mathbf{T} = \mathbf{T}^s + \mathbf{T}^p$ is composed of solvent $\mathbf{T}^s = 2\beta\mathbf{D}$ and polymer $\mathbf{T}^p$ contributions. The inertia terms may be safely ignored and play no role near corners, in much the same way as discussed for Newtonian flows [42]. We adopt a geometry with polar coordinates (r, θ) centred locally at the re-entrant corner, where $\theta = 0$ is the upstream wall and $\theta = \alpha$ being the downstream wall ($\pi < \alpha < 2\pi$). We perform the analysis generally for any corner angle greater than 180^o.

3.1 Matched asymptotic expansions

The asymptotic structure local to the sharp corner is comprised of three regions: an outer region away from the walls (which has been termed the core region, see Hinch [43] and Renardy [41]) and boundary layers at the upstream and downstream walls. The boundary layers are cusp like and in which viscometric behaviour dominates, whilst in the outer core region the polymer deforms affinely (with the relaxation and rate-of-strain terms being negligible). We use the ideas of Kaplun [34] and Van Dyke [35] to formulate the problem as a singular perturbation problem by using an artificial parameter based on radial distance from the singularity. The asymptotic expansions and matching then take place with respect to this parameter as it vanishes.

The analysis starts by considering the outer core region away from the walls. In order to impose a Newtonian velocity field, we must have that

$$1 \ll \mathbf{T}^p \ll \mathbf{T}^s \qquad \text{as } r \to 0, \tag{3.2}$$

so that the solvent stress dominates and (3.1) then reduces to Stokes equation

$$0 = -\nabla p + \beta\nabla^2\mathbf{v}. \tag{3.3}$$

The solution is given in [42, 44], and can be expressed as

$$\psi = C_0 r^{\lambda_0+1} f_0(\theta), \qquad p = C_0 r^{\lambda_0-1} g_0(\theta), \tag{3.4}$$

where ψ is the stream function, C_0 is an arbitrary constant and

$$f_0(\theta) = \frac{1}{2\lambda_0}\left(\frac{\cos\left((1-\lambda_0)\left(\theta-\frac{\alpha}{2}\right)\right)}{\cos\left((1-\lambda_0)\frac{\alpha}{2}\right)} - \frac{\cos\left((1+\lambda_0)\left(\theta-\frac{\alpha}{2}\right)\right)}{\cos\left((1+\lambda_0)\frac{\alpha}{2}\right)}\right), \tag{3.5}$$

$$g_0(\theta) = 2\frac{\sin\left((1-\lambda_0)\left(\theta-\frac{\alpha}{2}\right)\right)}{\cos\left((1-\lambda_0)\frac{\alpha}{2}\right)}. \tag{3.6}$$

The eigenvalue λ_0 is the positive root of the transcendental equation

$$\sin(\lambda_0\alpha) = -\lambda_0 \sin\alpha, \tag{3.7}$$

its value being $0.5 < \lambda_0 < 1$ for $\pi < \alpha < 2\pi$. The dominant behaviour of the polymer stress in this region takes the well known stretching form (see [43])

$$\mathbf{T}^p = \frac{(1-\beta)}{\mathrm{Wi}}\lambda(\psi)\,\mathbf{v}\mathbf{v}^T, \tag{3.8}$$

which is an exact solution of the upper convected stress derivative in (2.4) and λ is constant along streamlines. In fact (2.11)–(2.13) give that all three natural stress variables are constant along streamlines and taken in the power law forms

$$\lambda(\psi) = \frac{C_1}{C_0^2}\left(\frac{\psi}{C_0}\right)^{n_1}, \qquad \mu(\psi) = C_2\left(\frac{\psi}{C_0}\right)^{n_2}, \qquad \nu(\psi) = C_3 C_0^2\left(\frac{\psi}{C_0}\right)^{n_3}. \tag{3.9}$$

The exponents are fixed by matching to the boundary layers which determines

$$n_1 = \frac{2(\lambda_0 - 2)}{(3-\lambda_0)}, \qquad n_2 = \frac{(\lambda_0 - 1)}{(3-\lambda_0)}, \qquad n_3 = \frac{2}{(3-\lambda_0)}. \tag{3.10}$$

The constant C_0 is a free parameter in the solution, whilst the constants C_1, C_2, C_3 are determined by the solution of the upstream boundary layer and are fixed for given values of the corner angle. We thus have the order of magnitude estimates

$$\mathbf{v} = O(r^{\lambda_0}), \quad \nabla\mathbf{v} = O(r^{-(1-\lambda_0)}), \quad \mathbf{T}^s = O(r^{-(1-\lambda_0)}), \quad \mathbf{T}^p = O(r^{-\frac{4(1-\lambda_0)}{(3-\lambda_0)}}) \qquad \text{as } r \to 0. \tag{3.11}$$

These do indeed imply the dominance of the upper convected stress derivative in the constitutive equation (2.4) and moreover that the natural stress variables are constant along streamlines. However, (3.11) implies that $\mathbf{T}^s \ll \mathbf{T}^p$ in contradiction to (3.2), so that Newtonian flow is only appropriate when the polymer stresses are ignored in the momentum equation.

We now address the upstream boundary layer. Noting that the stream function has the limiting wall behaviour $\psi \sim C_0 x^{(\lambda_0-1)} y^2$ as $y \to 0^+$, we may deduce through dominant balance and matching to the outer core solution, the scalings for the boundary layer variables as

$$\begin{gathered} x = \epsilon\bar{X}, \qquad y = \epsilon^{(2-\lambda_0)}\bar{Y}, \qquad \psi = \epsilon^{(3-\lambda_0)}\bar{\Psi}, \\ T_{11}^p = \epsilon^{2(\lambda_0-1)}\bar{T}_{11}^p, \qquad T_{12}^p = \epsilon^{(\lambda_0-1)}\bar{T}_{12}^p, \qquad T_{22}^p = \bar{T}_{22}^p, \\ u = \epsilon\bar{u}, \qquad v = \epsilon^{2-\lambda_0}\bar{v}, \qquad \lambda = \epsilon^{2(\lambda_0-2)}\bar{\lambda}, \qquad \mu = \epsilon^{(\lambda_0-1)}\bar{\mu}, \qquad \nu = \epsilon^2\bar{\nu}, \end{gathered} \tag{3.12}$$

introducing an artificial small parameter ϵ to represent the radial lengths on which we are working. This approach has been developed for UCM and Oldroyd-B fluids in [48, 49], the small parameter ϵ being used as a gauge to give the asymptotic sizes of the variables. The scalings in (3.12) follow from dominant balance of the constitutive equations to give the boundary layer equations below and matching to the outer (core) solution (3.4) and (3.8). At leading order (in ϵ), these give the polymer stress boundary layer equations in Cartesian form as

$$\bar{T}_{11}^p + \mathrm{Wi}\left(\bar{u}\frac{\partial\bar{T}_{11}^p}{\partial\bar{X}} + \bar{v}\frac{\partial\bar{T}_{11}^p}{\partial\bar{Y}} - 2\frac{\partial\bar{u}}{\partial\bar{X}}\bar{T}_{11}^p - 2\frac{\partial\bar{u}}{\partial\bar{Y}}\bar{T}_{12}^p\right) = 0, \tag{3.13}$$

$$\bar{T}_{22}^p + \mathrm{Wi}\left(\bar{u}\frac{\partial\bar{T}_{22}^p}{\partial\bar{X}} + \bar{v}\frac{\partial\bar{T}_{22}^p}{\partial\bar{Y}} - 2\frac{\partial\bar{v}}{\partial\bar{Y}}\bar{T}_{22}^p - 2\frac{\partial\bar{v}}{\partial\bar{X}}\bar{T}_{12}^p\right) = 2(1-\beta)\frac{\partial\bar{v}}{\partial\bar{Y}}, \tag{3.14}$$

$$\bar{T}_{12}^p + \mathrm{Wi}\left(\bar{u}\frac{\partial\bar{T}_{12}^p}{\partial\bar{X}} + \bar{v}\frac{\partial\bar{T}_{12}^p}{\partial\bar{Y}} - \frac{\partial\bar{v}}{\partial\bar{X}}\bar{T}_{11}^p - \frac{\partial\bar{u}}{\partial\bar{Y}}\bar{T}_{22}^p\right) = (1-\beta)\frac{\partial\bar{u}}{\partial\bar{Y}}, \tag{3.15}$$

or equivalently for the natural stress variables as

$$(\bar{\mathbf{v}}.\bar{\nabla})\bar{\lambda} + 2\bar{\mu}\frac{\partial}{\partial\bar{Y}}\left(\frac{1}{\bar{u}}\right) + \frac{\bar{\lambda}}{\mathrm{Wi}} = 0, \tag{3.16}$$

$$(\bar{\mathbf{v}}.\bar{\nabla})\bar{\mu} + \bar{\nu}\frac{\partial}{\partial\bar{Y}}\left(\frac{1}{\bar{u}}\right) + \frac{\bar{\mu}}{\mathrm{Wi}} = 0, \tag{3.17}$$

$$(\bar{\mathbf{v}}.\bar{\nabla})\bar{\nu} + \frac{(\bar{\nu} - \bar{u}^2)}{\mathrm{Wi}} = 0, \tag{3.18}$$

with the two statements being connected by the relationships

$$\frac{\mathrm{Wi}}{(1-\beta)}\bar{T}^p_{11} = \bar{\lambda}\bar{u}^2, \qquad \frac{\mathrm{Wi}}{(1-\beta)}\bar{T}^p_{12} = \bar{\lambda}\bar{u}\bar{v} + \bar{\mu}, \qquad \frac{\mathrm{Wi}}{(1-\beta)}\bar{T}^p_{22} = -1 + \bar{\lambda}\bar{v}^2 + \frac{2\bar{\mu}\bar{v}}{\bar{u}} + \frac{\bar{\nu}}{\bar{u}^2}. \tag{3.19}$$

In these boundary layer equations, the stream function and velocity components are given exactly by

$$\bar{\Psi} = C_0\bar{X}^{\lambda_0-1}\bar{Y}^2, \qquad \bar{u} = 2C_0\bar{X}^{\lambda_0-1}\bar{Y}, \qquad \bar{v} = (1-\lambda_0)C_0\bar{X}^{\lambda_0-2}\bar{Y}^2. \tag{3.20}$$

The boundary layer equations are completed with suitable wall and far-field conditions, which for the natural stress equations (3.16)–(3.18) are

$$\text{as } \bar{Y}\to 0^+, \qquad \bar{\lambda} \sim \frac{2\mathrm{Wi}^2}{\bar{u}^2}\left(\frac{\partial\bar{u}}{\partial\bar{Y}}\right)^2, \quad \bar{\mu} \sim \mathrm{Wi}\frac{\partial\bar{u}}{\partial\bar{Y}}, \quad \bar{\nu}\sim\bar{u}^2. \tag{3.21}$$

$$\text{as } \bar{Y}\to +\infty, \qquad \bar{\lambda} \sim \frac{C_1}{C_0^2}\left(\frac{\bar{\Psi}}{C_0}\right)^{\frac{2(\lambda_0-2)}{(3-\lambda_0)}}, \quad \bar{\mu} \sim C_2\left(\frac{\bar{\Psi}}{C_0}\right)^{\frac{(\lambda_0-1)}{(3-\lambda_0)}}, \quad \bar{\nu} \sim C_3C_0^2\left(\frac{\bar{\Psi}}{C_0}\right)^{\frac{2}{(3-\lambda_0)}}, \tag{3.22}$$

The wall condition (3.21) represents viscometric stress behaviour, which in Cartesian variables takes the more familiar form

$$\text{as } \bar{Y}\to 0^+, \qquad \bar{T}^p_{11} \sim 2(1-\beta)\mathrm{Wi}\left(\frac{\partial\bar{u}}{\partial\bar{Y}}\right)^2, \quad \bar{T}^p_{12} \sim (1-\beta)\frac{\partial\bar{u}}{\partial\bar{Y}}, \quad \bar{T}^p_{22} \sim 2(1-\beta)\frac{\partial\bar{v}}{\partial\bar{Y}}. \tag{3.23}$$

The far-field conditions (3.22) are the matching conditions with the outer/core solution (3.9) and give a more accurately description than the stretching solution (3.8), by including the contributions of the two other natural stress variables. To obtain the same accuracy in the Cartesian formulation, requires proceeding to further terms in the outer expansion, which is tedious. As such, the analysis is now completed with reference to the use of the natural stress formulation only. It is also worth remarking that the boundary layer equations (3.13)–(3.15) or (3.16)–(3.18) are precisely the same equations that have been noted in [45] to arise for high Weissenberg number flows, their appearance here for $Wi = O(1)$ being a consequence of the singularity.

The boundary layer equations (3.16)–(3.18) with (3.21) and (3.22) admit the similarity solution

$$\xi = (-C_0\mathrm{Wi})\frac{\bar{Y}}{\bar{X}^{(2-\lambda_0)}}, \quad \bar{\lambda} = C_0^2\mathrm{Wi}^4\bar{X}^{2(\lambda_0-2)}\tilde{\lambda}(\xi), \quad \bar{\mu} = (-C_0\mathrm{Wi})\bar{X}^{(\lambda_0-1)}\tilde{\mu}(\xi), \quad \bar{\nu} = \frac{\bar{X}^2}{\mathrm{Wi}^2}\tilde{\nu}(\xi), \tag{3.24}$$

which conveniently scales both the stream function coefficient C_0 and Weissenberg out of the problem statement, giving

$$(3-\lambda_0)\xi^2\tilde{\lambda}' + (1+4(2-\lambda_0)\xi)\tilde{\lambda} + \frac{\tilde{\mu}}{\xi^2} = 0, \tag{3.25}$$

$$(3-\lambda_0)\xi^2\tilde{\mu}' + (1+2(1-\lambda_0)\xi)\tilde{\mu} + \frac{\tilde{\nu}}{2\xi^2} = 0, \tag{3.26}$$

$$(3-\lambda_0)\xi^2\tilde{\nu}' + (1-4\xi)\tilde{\nu} = 4\xi^2, \tag{3.27}$$

$$\text{as } \xi\to 0^+ \qquad \tilde{\lambda} \sim \frac{2}{\xi^2}, \quad \tilde{\mu}\sim -2, \quad \tilde{\nu}\sim 4\xi^2, \tag{3.28}$$

$$\text{as } \xi\to +\infty \qquad \tilde{\lambda} \sim C_1^*\xi^{\frac{4(\lambda_0-2)}{(3-\lambda_0)}}, \quad \tilde{\mu}\sim C_2^*\xi^{\frac{2(\lambda_0-1)}{(3-\lambda_0)}}, \quad \tilde{\nu}\sim C_3^*\xi^{\frac{4}{(3-\lambda_0)}}, \tag{3.29}$$

where $'$ denotes $d/d\xi$. The far-field similarity parameters are

$$C_1^* = C_1(-C_0\mathrm{Wi})^{-\frac{4}{(3-\lambda_0)}}, \qquad C_2^* = C_2(-C_0\mathrm{Wi})^{-\frac{(1+\lambda_0)}{(3-\lambda_0)}}, \qquad C_3^* = C_3(-C_0\mathrm{Wi})^{\frac{2(1-\lambda_0)}{(3-\lambda_0)}}. \tag{3.30}$$

The self-similar form of the downstream boundary layer equations may be deduced from (3.25)–(3.29) using the transformation

$$\xi \mapsto -\xi, \qquad \tilde{\mu}\mapsto -\tilde{\mu},$$

which gives the statement

$$(3-\lambda_0)\xi^2\tilde{\lambda}' - (1-4(2-\lambda_0)\xi)\tilde{\lambda} + \frac{\tilde{\mu}}{\xi^2} = 0, \tag{3.31}$$

$$(3-\lambda_0)\xi^2\tilde{\mu}' - (1-2(1-\lambda_0)\xi)\tilde{\mu} + \frac{\tilde{\nu}}{2\xi^2} = 0, \tag{3.32}$$

$$(3-\lambda_0)\xi^2\tilde{\nu}' - (1+4\xi)\tilde{\nu} = -4\xi^2, \tag{3.33}$$

$$\text{as } \xi \to 0^+ \qquad \tilde{\lambda} \sim \frac{2}{\xi^2}, \quad \tilde{\mu} \sim 2, \quad \tilde{\nu} \sim 4\xi^2, \tag{3.34}$$

$$\text{as } \xi \to +\infty \qquad \tilde{\lambda} \sim C_1^* \xi^{\frac{4(\lambda_0-2)}{(3-\lambda_0)}}, \quad \tilde{\mu} \sim -C_2^* \xi^{\frac{2(\lambda_0-1)}{(3-\lambda_0)}}, \quad \tilde{\nu} \sim C_3^* \xi^{\frac{4}{(3-\lambda_0)}}. \tag{3.35}$$

The upstream and downstream systems may both be solved as initial-value problems (IVP). The upstream case uses the wall condition (3.28) as the initial condition and integrates (3.25)–(3.29) into the far-field. In contrast, the downstream equations (3.31)–(3.33) use (3.35) as the initial condition and integrates into the wall behaviour (3.34). Figure 1 shows numerical results using Matblab's ode15s solver with tolerances $RelTol = AbsTol = 10^{-13}$ over the interval $[\xi_0, \xi_\infty]$, with $x_0 = 10^{-6}$ and $x_\infty = 10^{10}$ used in both upstream and downstream cases. It is convenient to use the scaled natural stress variables

$$\ell(\xi) = \xi^2\tilde{\lambda}, \qquad m(\xi) = \tilde{\mu}, \qquad n(\xi) = \frac{\tilde{\nu}}{\xi^2}, \tag{3.36}$$

which then take finite, non-zero values at the walls. Figure 1(a) shows the variables (3.36) scaled with their far-field behaviours from (3.29), illustrating convergence to the far-field constants (3.30) in the benchmark case of $\alpha = 270^o$, with convergence to the downstream wall behaviour being shown in Figure 1(b).

3.2 Confirmation using streamline integration

We may verify the exponents for the analytical stress behaviours predicted by (3.9) and (3.11) by integrating the constitutive equations along the given Newtonian streamlines. Since the stream function in (3.4) is expressed in polar coordinates, it is convenient to use the polar form of the constitutive equation instead of the Cartesian form (2.6)–(2.8). As such, we have

$$\begin{aligned}
&(\mathbf{v}.\nabla)T^p_{rr} - 2\frac{\partial v_r}{\partial r}T^p_{rr} - \frac{2}{r}\frac{\partial v_r}{\partial \theta}T^p_{r\theta} + \frac{T^p_{rr}}{\mathrm{Wi}} = \frac{2}{\mathrm{Wi}}\frac{\partial v_r}{\partial r},\\
&(\mathbf{v}.\nabla)T^p_{r\theta} + \frac{v_\theta}{r}T^p_{rr} - \frac{1}{r}\frac{\partial v_r}{\partial \theta}T^p_{\theta\theta} - \frac{\partial v_\theta}{\partial r}T^p_{rr} + \frac{T^p_{r\theta}}{\mathrm{Wi}} = \frac{1}{\mathrm{Wi}}\left(\frac{1}{r}\frac{\partial v_r}{\partial \theta} - \frac{v_\theta}{r} + \frac{\partial v_\theta}{\partial r}\right),\\
&(\mathbf{v}.\nabla)T^p_{\theta\theta} + 2\frac{v_\theta}{r}T^p_{r\theta} - 2\frac{\partial v_\theta}{\partial r}T^p_{r\theta} - \frac{2}{r}\frac{\partial v_\theta}{\partial \theta}T^p_{\theta\theta} - 2\frac{v_r}{r}T^p_{\theta\theta} + \frac{T^p_{\theta\theta}}{\mathrm{Wi}} = \frac{2}{\mathrm{Wi}}\left(\frac{1}{r}\frac{\partial v_\theta}{\partial \theta} + \frac{v_r}{r}\right),
\end{aligned} \tag{3.37}$$

with the velocity components being

$$v_r = \frac{1}{r}\frac{\partial \psi}{\partial \theta} = C_0 r^{\lambda_0} f'(\theta), \qquad v_\theta = -\frac{\partial \psi}{\partial r} = -C_0(1+\lambda_0)r^{\lambda_0} f(\theta).$$

Parameterising along streamlines using θ, the derivative $\mathbf{v}\cdot\nabla$ becomes the total derivative $r^{-1}v_\theta\, d/d\theta$ and (3.37) reduces to a set of odes along the streamline $r = (\psi/C_0 f(\theta))^{1/(1+\lambda_0)}$. In a similar manner so do (2.11)–(2.13) for the natural stress variables, where

$$\nabla.\mathbf{w} = \frac{1}{|\mathbf{v}|^4}\left((v_\theta^2 - v_r^2)\big(\frac{\partial v_\theta}{\partial r} + \frac{1}{r}\frac{\partial v_r}{\partial \theta} - \frac{v_\theta}{r}\big) + 4v_r v_\theta \frac{\partial v_r}{\partial r}\right)$$

and $|\mathbf{v}|^2 = v_r^2 + v_\theta^2$.

In the benchmark case of $\alpha = 270^o$, the Newtonian eigenvalue is $\lambda = 0.5445$ and the stress behaviours (3.9) and (3.11) are

$$\mathbf{T}^p = O(r^{-0.7420}), \qquad \lambda = O(r^{-1.8310}), \qquad \mu = O(r^{-0.2865}), \qquad \nu = O(r^{1.2580}). \tag{3.38}$$

These are verified in Figure 2, confirming the singularity behaviour along the line $\theta = \pi/2$.

3.3 Comparison to the true viscoelastic velocity field

In a fixed Newtonian velocity field, (3.11) summarise the velocity and stress behaviours at the singularity. In addition, we have the wall boundary thickness estimates of $O(r^{2-\lambda_0})$. These should be contrasted with the corresponding results, when the velocity field is no longer artificially fixed, but allowed to adapt so that the momentum equation is satisfied. In this case, the velocity field is given by a potential flow solution, which is a consequence of the polymer stretching solution (3.8) still pertaining, but now the momentum equation yielding a form of Euler's equation. The coupled flow and stress fields through the analysis in [43, 46, 47] and [48, 49, 50, 51] are shown to satisfy

$$\mathbf{v} = O(r^{(3-\frac{\pi}{\alpha})\frac{\pi}{\alpha}-1}), \quad \mathbf{T}^s = O(\nabla\mathbf{v}) = O(r^{-(1-\frac{\pi}{\alpha})(2-\frac{\pi}{\alpha})}), \quad \mathbf{T}^p = O(r^{-2(1-\frac{\pi}{\alpha})}) \qquad \text{as } r \to 0, \tag{3.39}$$

away from the walls. The specific form of the stream function here is

$$\psi = C_0 \left(r^{\frac{\pi}{\alpha}} \sin\left(\frac{\pi}{\alpha}\theta\right)\right)^{3-\frac{\pi}{\alpha}}. \tag{3.40}$$

Again wall boundary layers appear, but now of thickness of $O(r^{(2-\frac{\pi}{\alpha})})$. In the benchmark case of $\alpha = 3\pi/2$, we have that

$$\mathbf{v} = O(r^{5/9}), \quad \mathbf{T}^s = O(\nabla\mathbf{v}) = O(r^{-4/9}), \quad \mathbf{T}^p = O(r^{-2/3}).$$

The exponents for the velocity and solvent stress are very similar to their values in the Newtonian velocity field. However the polymer stress we note is less singular than its corresponding behaviour in (3.38) and the boundary layer thicknesses are $O(r^{4/3})$, which are slightly narrower than those in the Newtonian velocity case of $O(r^{1.4555})$. Thus the Newtonian velocity field, actually produces a stronger stress singularity than the true viscoelastic velocity field.

4 The 4:1 contraction flow

The numerical methodology employed to discretize the continuity and momentum equations (2.1)–(2.2) and the constitutive equations (2.6)–(2.8) for CSF and (2.15)–(2.17) for NSF, is the Finite Difference Method in the context of a staggered grid. In particular, the flow equations (2.2) are solved via a projection method while the constitutive equations are obtained via an explicit time discretization. In the present work, all convective terms of the equations are approximated by the CUBISTA scheme which is described in detail for non-uniform meshes in [52]. More details about the numerical methodologies of CSF and NSF including the verification of the code can be found in our previous work [37].

The focus of this work is the solution of the $4:1$ contraction flow, which is illustrated in Fig. 3a). In particular we have adopted $20L$ length for each channel, with non-uniform cell distributions around the re-entrant corners as shown in Fig. 3b).

4.1 Numerical results in a Newtonian velocity field

The investigations in this Section use only a Newtonian velocity field ($\gamma = 0$ in Eq. (2.2)) with simulations run on the meshes described in Table 1 for the parameter values $\mathrm{Re} = 0.01$, $\mathrm{Wi} = 1$ and $\beta = 1/9$.

4.1.1 Temporal convergence

We describe first, the temporal convergence of CSF and NSF schemes. The mesh adopted is $M1$, as described in Table 1. The behaviour of the components of the Cartesian stress tensor and the NS variables around the singularity is studied through the local residuals as a function of time, for selected fixed time-steps. In particular, the local residuals are captured at a control point Z located in the closest cell to the singularity. For instance, the component 11 of the extra stress tensor and the $\hat{\lambda}$ NS variable are respectively evaluated as

$$\begin{aligned} res(T_{11}^P)|_Z = & \left.\frac{(T_{11}^P)^{(n+1)} - (T_{11}^P)^{(n)}}{\delta t}\right|_Z + \left.\left(u\frac{\partial T_{11}^P}{\partial x} + v\frac{\partial T_{11}^P}{\partial y}\right)\right|_Z^{(n+1)} - \left.\left(2\frac{\partial u}{\partial x}T_{11}^P + 2\frac{\partial u}{\partial y}T_{12}^P\right)\right|_Z^{(n+1)} \\ & + \left.\frac{T_{11}^P}{\mathrm{Wi}}\right|_Z^{(n+1)} - \left.\frac{2}{\mathrm{Wi}}(1-\beta)\frac{\partial u}{\partial x}\right|_Z^{(n+1)}, \end{aligned} \tag{4.41}$$

and

$$\begin{aligned} res(\hat{\lambda})|_Z = & \left.\frac{\hat{\lambda}^{(n+1)} - \hat{\lambda}^{(n)}}{\delta t}\right|_Z + \left.\left(\frac{2\hat{\mu}}{|\mathbf{v}|^2}\left(v\frac{\partial u}{\partial t} - u\frac{\partial v}{\partial t}\right)\right)\right|_Z^{(n+1)} + \left.\left(|\mathbf{v}|^2(\mathbf{v}\cdot\nabla)\left(\frac{\hat{\lambda}}{|\mathbf{v}|^2}\right)\right)\right|_Z^{(n+1)} \\ & + \left(2\hat{\mu}|\mathbf{v}|^2\nabla\cdot\mathbf{w}\right)\Big|_Z^{(n+1)} + \left.\left(\frac{1}{\mathrm{Wi}}\left(\hat{\lambda}-1\right)\right)\right|_Z^{(n+1)}, \end{aligned} \tag{4.42}$$

where the local residuals for the other components of the extra stress tensor and for the remaining NS variables can be constructed in a similar manner. In particular, the local residual investigation is done for the time-steps $\delta t = 10^{-4}, 5\times10^{-5}$ and 10^{-5}.

Fig. 4 shows the time variation of the local residuals on a logarithm scale, verifying that both formulations are convergent with similar decay rates. For the $\hat{\mu}$ and $\hat{\nu}$ variables using $\delta t = 10^{-4}$ and $\delta t = 10^{-5}$, there are slight oscillations when the residuals become small.

4.1.2 Global behaviour

The second round of comparisons considers the global behaviour of the properties away from the re-entrant corner. In Fig. 5, we have plotted the results for the u-component of the velocity field, the pressure field and the first normal stress difference ($N_1 = T_{22}^P - T_{11}^P$) along the centreline of the contraction, for instance at $y = 0$. For the variables u and p in Figs. 5 a) and b), we have the exact same values for both formulations since we are using the same Newtonian velocity field. For the N_1 variable both formulations show excellent agreement.

Another study of interest is analysing the flow type parameter (ft) defined by

$$\mathrm{ft} = \frac{|\frac{1}{2}(\nabla\mathbf{v} + (\nabla\mathbf{v})^T)| - |\frac{1}{2}(\nabla\mathbf{v} - (\nabla\mathbf{v})^T)|}{|\frac{1}{2}(\nabla\mathbf{v} + (\nabla\mathbf{v})^T)| + |\frac{1}{2}(\nabla\mathbf{v} - (\nabla\mathbf{v})^T)|}. \tag{4.43}$$

This may be used for identifying the type of local flow dominating in spatial locations, where ft $= -1$ implies solid-like rotation, ft $= 1$ characterizes pure extensional flow, and ft $= 0$ represents pure shear flow. Results for the contour map of ft are presented in Fig. 6. Figure 7 gives a zoom perspective in the vicinity of the re-entrant corner. It is interesting to note that the Newtonian velocity field maintains the same main local types of flow seen in [12] for the fully viscoelastic flow field, i.e. extensional flow around the salient corner and in the centreline of the first channel of the contraction, the solid-like rotation behaviour around the re-entrant corner and shear flow around the wall of the downstream channel and in the remainder of the upstream channel.

4.1.3 Spatial convergence near the singularity

We now compare the numerical and asymptotic results in the 4 : 1 contraction flow using the meshes presented in Table 1. As the main objective of this Section is to present for the literature a new benchmark test focusing on the re-entrant corner and the stress singularity behaviour, we have assumed the same flow condition employed in the asymptotic analysis of section 3.1, i.e., the numerical schemes were solved using $\gamma = 0$ in Eq. (2.2). The asymptotics results provided by [44, 42] for the velocity field and hence the solvent stress are discussed in detail in section 3 and give that in the vicinity of the re-entrant corner the elastic stress tensor behaves as (3.38).

In order to present a detailed comparison with the asymptotic results, the numerical solutions are plotted along radial lines for three different values of θ (see Fig. 8), specifically $\theta = \pi/2, \pi$ and $3\pi/4$. It is worth noting that the θ angle is measured from the downstream wall, in contrast to the asymptotics in section 3 which measures it from the upstream wall. Fig. 9 shows that the NSF results are in excellent agreement with the asymptotic results given in (3.38) in contrast with those produced by CSF. According to the first column of Fig. 9, we can see that the CSF converges slower to its asymptotics than the NSF evidencing the need for a very fine mesh for this formulation to capture the correct asymptotics. In particular, for $\theta = \pi$, the CSF struggles with the T^p_{22} component. These results confirm the accuracy of the NSF in re-entrant corner flows, as demonstrated initially by Renardy [39].

4.1.4 Boundary layer structures

We may further explore the stress singularity by examining numerically the boundary layer structures at the walls local to the re-entrant corner. For this, we compare the absolute magnitude of the main groups of terms in the constitutive equations (2.4), i.e., we investigate

$$\max\left(\frac{|\mathbf{T}^p_{ij}|}{Wi}, |\overset{\triangledown}{\mathbf{T}}{}^p_{ij}|, \frac{2(1-\beta)}{Wi}|\mathbf{D}_{ij}|\right), \tag{4.44}$$

for each of the three components $ij = 11, 12$ and $= 22$ separately. This study is also conducted for NSF since the elastic extra-stress tensor $\mathbf{T}^p$ can be recovered from NS variables using the relationships Eqs. (2.18)–(2.20). Results are presented in Fig. 10 where in these figures, we have considered a specific region near to the singularity, the maps being labeled without the presence of the modulus sign for convenience. In the first column of this figure, results for CSF are described for each component while in the second column of Fig. 10 we have results using the NS variables. Notice that for component 11, as described in Figs. 10a) and b) by blue representations, both formulations show the dominance of the upper convective polymer stress derivative in the vicinity of the geometrical singularity. Comparing Figs. 10c) and e) with Figs. 10d) and f), we can see that the NSF more adequately captures the boundary layer structures, since very close to the singularity, the term $\overset{\triangledown}{\mathbf{T}}{}^p$ more strongly dominates for the components 12 and 22. For both formulations, the stress boundary layers are evident at both upstream and downstream walls, where either rate of strain or the relaxation terms dominate, as must be required for viscometric behaviour. In summary the results are in agreement with the expected asymptotic results from Eqs. (3.13) – (3.14).

4.2 Comparison with the true viscoelastic velocity case

4.2.1 Temporal convergence

We begin with comparisons related to the simulations considering the viscoelastic velocity field, so that $\gamma = 1$ in Eq. (2.2). Again, the mesh adopted for this study is $M1$. As well explained in our previous work [37], the pure NSF imposes a severe space step restriction in simulations combining the true viscoelastic velocity field with a small viscosity ratio $\beta = 1/9$. Therefore, for the viscoelastic velocity field simulations, we have adopted the hybrid version proposed in [37]. Fig. 11 shows that both formulations are convergent and that the oscillations present in some time steps for the Newtonian velocity case are corrected. Of particular note are the faster convergence rate of the NSF stresses.

4.2.2 Global behaviour

Figures 12(a) and (c) confirm, as in the Newtonian velocity case, that both formulations produce practically identical results for u and $T_{22}^P - T_{11}^P$. However, as presented in Fig. 12 (b), it is evident that the profile for the pressure field is highly dependent on the formulation in the viscoelastic case. As expected, the solutions for both CSF and NSF in the viscoelastic velocity field increase the values of the pressure drop as compared with those using the Newtonian velocity field.

According to Fig. 13, we note that both CSF and NSF formulations in the viscoelastic velocity field produce similar results to those plotted in Fig. 6 for the Newtonian velocity. However, a noteworthy difference can be seen in the narrower channel, where extension now remains high along the centre of the channel. Moreover, as we can see in Figs. 7 and 14, there are noticeable differences between the application of the two different velocity fields around the salient and re-entrant corners. In particular, the NSF hybrid version with viscoelastic velocity increases the solid-like rotation flow type around the singularity in the re-entrant corner.

4.2.3 Boundary layer structures

A comparison between numerical (CSF and NSF) and asymptotic results near to the singularity in the viscoelastic velocity field was presented in our previous work [37]. We augment those results here by presenting the maps for the boundary layer structures.

Figure 15 shows better agreement with the theoretical asymptotic structure for CSF than in the Newtonian velocity case. It is still noteworthy that NSF produces a larger region of dominance for the upper convected stress derivative than CSF (which is still relatively absent for the 22 component of CSF, whilst it is correctly caught for this components by NSF). In both formulations, evidence of the stress boundary layers at the walls are again indicated through the dominance of the rate-of-strain or relaxation terms (both being required for correct viscometric behaviour).

5 The stick-slip problem

The stick-slip flow is a benchmark problem for viscoelastic models due to the presence of the stick-slip transition point (also termed as separation point) where the stress singularity is located. In summary, at this point, there is a sudden modification in the boundary condition of the flow: the no-slip boundary condition for the velocity field at the die wall changes to a zero shear stress free-surface condition, along which the fluid slips.

The main purpose of our study in this Section is to offer to the computational rheology community a detailed investigation concerning the numerics and asymptotics for a viscoelastic free surface flow under Newtonian kinematics. The stick-slip problem, in which the free surface remains flat after the die exit, can be used as a preliminary code validation to implement the complex die-swell problem [54, 21]. In the context of the viscoelastic kinematics and steady-state flow, the stick-slip problem has been numerically investigated by Fortin et al. [55], Baaijens [56], Xue et al. [57] and Karapetsas & Tsamopoulos [20]. More recently, a careful investigation for viscoelastic transient flows has been presented in our previous work [53] analysing the numerics and asymptotics around the stress singularity at the stick-slip point. However, in that work, the numerical investigations focused on the Phan-Thien–Tanner and Giesekus models, and did not consider the Oldroyd-B model. Therefore, in order to describe further numeric and asymptotic comparisons for completeness, in this Section we have also included the Cartesian and the Natural stress behaviors for the Oldroyd-B model with Newtonian kinematics.

A description of the flow geometry for the stick-slip problem is illustrated in Fig. 16 while the meshes adopted for all simulations are described in Table 2. In order to present a comparison between numerical and asymptotic results, we first consider the full simulation of the stick-slip problem under a Newtonian velocity field ($\gamma = 0$ in Eq. (2.2)) using the Oldroyd-B model with Re $= 0.01$, Wi $= 1$ and $\beta = 1/9$. As presented in our previous work [36], assuming the Newtonian kinematics for an Oldroyd-B fluid, the

asymptotic results for the stick-slip problem behave as

$$\mathbf{T}^p = O(r^{-4/5}), \qquad \lambda = O(r^{-9/5}), \qquad \mu = O(r^{-3/10}), \qquad \nu = O(r^{6/5}), \tag{5.45}$$

where r is the radial distance from the singularity.

This investigation is conducted analysing the solution in three different angle values around the stick-slip transition point, specifically $\theta = \frac{\pi}{4}$, $\theta = \frac{\pi}{2}$ and $\theta = \frac{3\pi}{4}$, as illustrated in Fig. 17. According to Fig. 18, the numerical results for NS variables λ, μ and ν are in excellent agreements with the expected asymptotic results in all selected angles. As described in the first column of Fig. 18, we note that the CSF results are convergent and in satisfactory agreement with the theory. However, as can be seen in Fig. 18, the NSF captures the asymptotics more accurately than the CSF.

As a further investigation, we carry out a numerical study concerning the stress behaviour on the slip surface. Particularly, we have plotted in Fig. 19 the stress profile of T^P_{11} along the top slip surface, i.e., fixing $y = 1$ (see Fig. 16) and varying the horizontal length $x \in [-8L, 8L]$. Besides the result for the Oldroyd-B model, in this numerical investigation we have also included the results for the PTT and Giesekus fluids. In order to save space, we have omitted the governing equations for theses models since it can be found in our previous work [53]. Figure 19 indicates that the value of T^P_{11} around the singularity for Oldroyd-B fluid is greater than those obtained by PTT and Giesekus models. These behaviours for the models numerically confirm the analysis presented in [36] for the stick-slip problem under Newtonian kinematics: namely that the Oldroyd-B model extends the point singularity at the join of the stick and slip surfaces to the whole of slip surface, whilst the PTT and Giesekus models can stop the continual stress growth on the slip surface.

Finally, as for the contraction flow in the previous section, we present in Fig. 20 the boundary layer structures for the stick-slip problem. According to Fig. 20(c)-(f), for the components $ij = 12$ and $= 22$ both formulations captured the dominance of the upper convective polymer stress derivative (blue representation) near the singularity but away from the stick and slip boundaries. This behaviour is not observed for component $ij = 11$.

6 The cross-slot flow

Relatively recently, the computational rheology community has adopted a new benchmark for investigating asymmetric flow instabilities: the cross-slot problem [58, 59]. The geometry considered for this flow is formed by crossed channels, and an important issue concerns the numerical behavior of the stresses in the vicinity of the internal stagnation point. It appears that the natural stress formulation has yet to be used on this problem. Therefore, in this section, we numerically investigate the behavior of the natural stress variables at the stagnation region for Newtonian kinematics.

The meshes used in the numerical simulations have 50 and 200 cells in the central square region of the cross slot along x and y directions, respectively denoted here as M1 ($\delta x_{min} = \delta y_{min} = 0.02$) and M2 ($\delta x_{min} = \delta y_{min} = 0.005$). The remaining data is based on the benchmark paper of Cruz et al. [59]: the Reynolds number is $Re = 0.01$, the ratio of viscosity is $\beta = 1/9$, and the Deborah numbers (or Weissenberg number) are $De = 0.3$ and $De = 0.36$. Noteworthy, is that the authors in [59] adopted these reference De values to investigate the transition of a steady symmetric to a steady non-symmetric flow for the Oldroyd-B model and a viscoelastic velocity field. However, in the current work, as we are adopting a Newtonian velocity field for solving the NSF, the flow is always symmetric, i.e., the streamlines for both values of De are similar to the pure Newtonian flow ($De = 0$).

In order to clarify the numerical behavior of the NSF for dealing a flow with an internal stagnation point, in Fig. 21 we have plotted the results for the NS variables λ, ν and μ as function of x at $y = 0$. We have also included in this figure (see first column of Fig. 21) the results for the components of the Cartesian stress tensor. An important consideration that can be seen in Fig. 21 is that the NS variables λ, ν and μ are respectively related to the Cartesian stress components T^P_{22}, T^P_{11} and T^P_{12}. Moreover, despite the application of the Newtonian kinetics for solving the NSF in the cross-slot flow, the behavior of λ is qualitatively in agreement with the behavior for the normal stress component T^P_{22}, i.e., increasing the

De number leads to an increasing of the value for this NS variable around the stagnation point. The mesh refinement in Fig. 21 is also indicating the numerical convergence of the both formulations in this benchmark problem.

As a further study, we present in Figs. 22 and 23 studies related to the dominant terms close to the stagnation point region for $De = 0.3$ and $De = 0.36$ respectively. Similarly as the contraction and stick-slip flows, this investigation is conducted applying Eq. (4.44) for each cell in the domain and for the stress components ij. In addition to the NSF results, in these figures we have also presented the results for CSF considering the Newtonian velocity. According to Figs. 22 and 23, we notice greater sensitivity of the NSF method to capture the presence of the stagnation point as compared with the results of the CSF for both De numbers. In particular, we can highlight that the dominance of the convected derivative in the vicinity of the stagnation point is more evident for NSF than for CSF. In order to confirm the potentiality of the NSF over CSF for stagnation point flows, new numerical results need be further investigated in future work using the viscoelastic velocity instead of the Newtonian kinematics.

7 Discussion

We have considered here two different viscoelastic formulations of the Oldroyd-B equations, and assessed these in contraction flow and stick-slip problem under a Newtonian velocity. The motivation for the fixed kinematics being that it is an intermediate case that decouples the constitutive and momentum equations.

In the context of the contraction flow, the numerical comparisons have been performed for Weissenberg unity, our intention being to compare the temporal and spatial convergence of the two formulations, particularly near the re-entrant corner stress singularity. The method of matched asymptotic expansions has been used to determine the structure and form of the singularity, the details presented here completing the initial analysis by Renardy [41]. The numerical results indicate that the NSF is able to capture more accurately, not only the stress singularity, but also the asymptotic structure local to the corner, including the stretching region (where the upper convected derivative of stress dominates) and the boundary layers at the walls.

We have noted that the stress behaviour of both formulations for Newtonian velocities share many similar flow characteristics to the viscoelastic velocity case. The re-entrant corner stress singularity is markedly different however, as it is stronger in the Newtonian velocity field. However, the global stress similarities between the two flow fields are expected to reduce as the Weissenberg number increases. In particular, the viscoelastic velocity field induces the appearance of a lip vortex at slightly higher Weissenberg numbers [7], which is never present for Newtonian velocities.

For the stick-slip problem, we have verified that the NSF can capture the asymptotics more accurately than the CSF. In addition, we have also shown the unbounded stress growth for the Oldroyd-B model in the vicinity of the slip surface, in contrast with the bounded behaviour for the PTT and Giesekus models.

Finally, the NSF has been applied in solving a flow with an internal stagnation point: the cross-slot problem. Considering a Newtonian velocity field and the region of stagnation point, the normal conformation stress component in the direction of flow along a streamline is λ behaves as the normal stress component T_{22}^P. In particular, this NS variable can capture the presence of the stagnation point as De is increased. Moreover, the interpretation of dominant terms in the cross-slot geometry is also presented. Summarily, these results for the cross-slot benchmark problem are indicating that NSF can be more accurate than the CSF in numerically solvling stagnation point flows. However, in order to give more evidence concerning this last statement, further studies must be conducted using the viscoelastic velocity field.

Acknowledgements

The authors would like to thank the financial support given by SPRINT/FAPESP grant no. 2018/22242-0. C.M. Oishi acknowledges CNPq (Conselho Nacional de Desenvolvimento Científico e Tecnologico), grant

no. 307459/2016-0 and FAPESP (Fundação de Amparo à Pesquisa do Estado de São Paulo) grants no. 2013/07375-0. I. L. Palhares Junior acknowledges the financial support of FAPESP grants no. 2014/17348-2 and BEPE no. 2016/20389-8.

References

[1] R. Keunings, On the high Weissenberg number problem. *J. Non-Newt. Fluid Mech.* 20:209–226 (1986).

[2] D. V. Boger, Viscoelastic flows through contractions. *Ann. Rev. Fluid Mech.* 19:157–182 (1987).

[3] R. J. Poole, M. A. Alves and P. J. Oliveira, Purely Elastic Flow Asymmetries. *Phys. Rev. Lett.* 99:164503 (2007).

[4] K. Walters and M. Webster, The distinctive CFD challenges of computational rheology, ECCOMAS Swansea 2001. *Int. J. Numer. Meth. Fluids.* 45:577–596 (2003).

[5] O. Hassager, Working group on numerical techaniques. Fifth International Workshop on Numerical Methods in Non-Newtonian Flows, Lake Arrowhead, USA. *J. Non-Newt. Fluid Mech.* 29:2–5 (1988).

[6] M. Aboubacar, H. Matallah and M. F. Webster, Highly elastic solutions for Oldroyd-B and Phan-Thien/Tanner fluids with a finite volume/element method: planar contraction flows. *J. Non-Newt. Fluid Mech.* 103:65–103 (2002).

[7] M. A. Alves, P. J. Oliveira and F. T. Pinho, Benchmark solutions for the flow of Oldroyd-B and PTT fluids in planar contractions. *J. Non-Newt. Fluid Mech.* 110:45–75 (2003).

[8] J. M. Kim, C. Kim, J. H. Kim, C. Chung, K. H. Ahn and S. J. Lee, High-resolution finite element simulation of 4:1 planar contraction flow of viscoelastic fluid. *J. Non-Newt. Fluid Mech.* 129:23–37 (2005).

[9] Y. Mu, G. Zhao, X. Wu and J. Zhai, Modeling and simulation of three-dimensional planar contraction flow of viscoelastic fluids with PTT, Giesekus and FENE-P constitutive models. *Appl. Math. Comput.* 218:8429-8443 (2012).

[10] H. C. Lee, A nonlinear weighted least-squares finite element method for the Oldroyd-B viscoelastic flow. *Appl. Math. Comput.* 219:421-434 (2012).

[11] C. Liu and S. Zhiyong, An incremental pressure correction finite element method for the time-dependent Oldroyd flows. *Appl. Math. Comput.*. 351:99-115 (2019).

[12] A. M. Afonso, P. J. Oliveira, F. T. Pinho, M. A. Alves, Dynamics of high-Deborah-number entry flows: a numerical study. *J. Fluid Mech.* 677:272–304 (2011).

[13] X. Chen, H. Marschall, M. Schafer, D. Bothe, A comparison of stabilization approaches for finite-volume simulation of viscoelastic fluid flow. *Int. J. Comput. Fluid Dyn.*. 27:229-250 (2013).

[14] E. Castilho and R. Codina, Variational multi-scale stabilized formulations for the stationary three-field incompressible viscoelastic flow problem. *Comput. Meth. Appl. Mech. Eng.* 279:579–605 (2014).

[15] M. Lukacova-Medvidova, H. Notsu, B. She, Energy dissipative characteristic schemes for the diffusive Oldroyd-B viscoelastic fluid. *Int. J. Numer. Meth. Fluids.* 41:47-75 (2015)

[16] J. L. Favero, A. R. Secchi, N. S. M. Cardozo, and H. Jasak, Viscoelastic flow analysis using the software OpenFOAM and differential constitutive equations. *J. Non-Newt. Fluid Mech.* 165:1625–1636 (2010).

[17] F. Pimenta and M. A. Alves, Stabilization of an open-source finite-volume solver for viscoelastic fluid flows. *J. Non-Newt. Fluid Mech.* 239:85–104 (2017).

[18] M. S. B. Araujo, C. Fernandes, L. L. Ferras, Z. Tukovic, H. Jasak, J. M. Nobrega, A stable numerical implementation of integral viscoelastic models in the OpenFOAM-computational library. *Comput. Fluids.* 172:728–740 (2018).

[19] J. D. Evans and C. M. Oishi, Transient computations using the natural stress formulation for solving sharp corner flows. *J. Non-Newt. Fluid Mech.* 249:48–52 (2017).

[20] G. Karapetsas and J. Tsamopoulos, On the stick-slip flow from slit and cylindrical dies of a phan-thien and tanner fluid model. i. steady state. *Phys. Fluids.* 21(12):123101 (2009).

[21] R. Comminal, F. Pimenta, J. H. Hattel, M. A. Alves and J. Spangenberg, Numerical simulation of the planar extrudate swell of pseudoplastic and viscoelastic fluids with the streamfunction and the VOF methods. *J. Non-Newt. Fluid Mech.*. 252:1–18 (2018).

[22] M. Renardy, Asymptotic structure of the stress field in flow past a cylinder at high Weissenberg number. *J. Non-Newt. Fluid Mech.* 79:387–403 (2000).

[23] P. Wapperom and M. Renardy, Numerical prediction of the boundary layers in the flow around a cylinder using a fixed velocity field. *J. Non-Newt. Fluid Mech.* 125:35–48 (2005).

[24] J. Rosenberg and R. Keunings, Numerical integration of differential viscoelastic models. *J. Non-Newt. Fluid Mech.* 39:269–290 (1991).

[25] A. Fortin, A. Zine and J.F. Agassant, Computing viscoelastic fluid flow problems at low cost. *J. Non-Newt. Fluid Mech.* 45:209–229 (1992).

[26] N. Phan-Thien and R.I. Tanner, A new constitutive equation derived from network theory. *J. Non-Newt. Fluid Mech.* 2:353–365 (1977).

[27] N. Phan-Thien, A nonlinear network viscoelastic model. *Trans. Soc. Rheol.* 22:259–283 (1978).

[28] H. Giesekus, A simple constitutive equation for polymer fluids based on the concept of deformation-dependent tensorial mobility. *J. Non-Newt. Fluid Mech.* 11:69–109 (1982).

[29] M. Renardy, Re-entrant corner behavior of the PTT fluid. *J. Non-Newt. Fluid Mech.* 69:99–104 (1997).

[30] J. D. Evans, Re-entrant corner behavior of the PTT fluid with a solvent viscosity. *J. Non-Newt. Fluid Mech.* 165:527–537 (2010).

[31] J. D. Evans, Re-entrant corner behavior of the Giesekus fluid with a solvent viscosity. *J. Non-Newt. Fluid Mech.* 165:538–543 (2010).

[32] J. D. Evans, Stick-slip and slip-stick singularities of the Phan-Thien–Tanner fluid. *J. Non-Newt. Fluid Mech.* 199:12–19 (2013).

[33] J. D. Evans, Stick-slip singularity of the Giesekus. *J. Non-Newt. Fluid Mech.* 222:24–33 (2015).

[34] S. Kaplun, *Fluid Mechanics and Singular Perturbation.* Academic Press, New York, 1967.

[35] M. Van Dyke, *Perturbation methods in fluid mechanics.* Academic Press, New York, 1964.

[36] J. Evans, I. L. Palhares Junior, and C. M. Oishi, Stresses of the Oldroyd-B, PTT and Giesekus fluids in a Newtonian velocity field near the stick-slip singularity. *Phys. Fluids.* 29:1–33 (2017).

[37] J. D. Evans, H. L. Franca, and C. M. Oishi, Application of the natural stress formulation for solving unsteady viscoelastic contraction flows. *J. Comput. Phys.* 388(1):424–489 (2019).

[38] C. M. Oishi, F. P. Martins, M. F. Tome, J. A. Cuminato, and S. Mckee, Numerical solution of the extended pom-pom model for viscoelastic free surface flows. *J. Non-Newt. Fluid Mech.* 166(3):165–179 (2011).

[39] M. Renardy, How to integrate the upper convected Maxwell (UCM) stresses near a singularity (and maybe elsewhere, too). *J. Non-Newt. Fluid Mech.* 52:91–95 (1994).

[40] S. Dupont, J. M. Marchal and M. J. Crochet, Finite element simulation of viscoelastic fluids of the integral type. *J. Non-Newt. Fluid Mech.* 17:157–183 (1985).

[41] M. Renardy, The stresses of an upper convected Maxwell fluid in a Newtonian velocity field near a re-entrant corner. *J.Non-Newt. Fluid Mech.* 50:127–134 (1993).

[42] H. K. Moffatt, Viscous and resistive eddies near a sharp corner *J. Fluid Mech.* 18:1–18 (1964).

[43] E. J. Hinch, The flow of an Oldroyd fluid around a sharp corner. *J. Non-Newt. Fluid Mech.* 50:161–171 (1993).

[44] W. R. Dean and P. E. Montagnon, On the steady motion of viscous liquid in a corner. *Proc. Cambridge Philos. Soc.* 45:389–394 (1949).

[45] T. Hagen and M. Renardy, Boundary layer analysis of the Phan-Thien-Tanner and Giesekus model in high Weissenberg number flow. *J. Non-Newt. Fluid Mech.* 73:181–189 (1997).

[46] M. Renardy, A matched solution for corner flow of the upper convected Maxwell fluid. *J. Non-Newt. Fluid Mech.* 58:83–89 (1995).

[47] J. M. Rallison and E. J. Hinch, The flow of an Oldroyd fluid past a reentrant corner: the downstream boundary layer. *J. Non-Newt. Fluid Mech.* 116:141–162 (2004).

[48] J. D. Evans, Re-entrant corner flows of the Upper Convected Maxwell fluid. *Proc. Roy. Soc. A.* 461:117-142 (2005).

[49] J. D. Evans, Re-entrant corner flows of the Oldroyd-B fluid. *Proc. Roy. Soc. A.* 461:2573–2603 (2005).

[50] J. D. Evans, Re-entrant corner flows of UCM fluids: The Cartesian stress basis. *J. Non-Newt. Fluid Mech.* 150:116-138 (2008).

[51] J. D. Evans, Re-entrant corner flows of UCM fluids: The natural stress basis. *J. Non-Newt. Fluid Mech.* 150:139-153 (2008).

[52] M. A. Alves, P. J. Oliveira and F. T. Pinho, A convergent and universally bounded interpolation scheme for the treatment of advection. *Int. J. Numer. Meth. Fluids.* 41:47–75 (2003).

[53] J. Evans, J. A. Cuminato, I. L. Palhares Junior, and C. M. Oishi, Numerical study of the stress singularity in stick-slip flow of the Phan-Thien Tanner and Giesekus fluids. *Phys. Fluids.* 31:093101 (2019).

[54] C.M. Oishi, F.P. Martins, M.F. Tome, J. A. Cuminato, and S. McKee, Numerical solution of the eXtended Pom-Pom model for viscoelastic free surface flows *J. Non-Newt. Fluid Mech.*. 166:165–179 (2011).

[55] A. Fortin, A. Zine, and J.-F. Agassant. Computing viscoelastic fluid flow problems at low cost. *J. Non-Newt. Fluid Mech.*, 45(2):209 – 229, (1992).

[56] F. P. T. Baaijens. Application of low-order discontinuous Galerkin methods to the analysis of viscoelastic flows. *J. Non-Newt. Fluid Mech.*, 52:37–57 (1994).

[57] S.-C. Xue, R. I. Tanner, and N. Phan-Thien. Three-dimensional numerical simulations of viscoelastic flows–predictability and accuracy. *Comput. Methods Appl. Mech. Engrg.*, 180:305–331, 1999.

[58] R.J. Poole, M.A. Alves and P.J. Oliveira. Purely elastic flow asymmetries. *Phys. Rev. Lett.*, 99:164503 (2007).

[59] F.A. Cruz, R.J. Poole, A.M. Afonso, F.T. Pinho, P.J. Oliveira and M.A. Alves. A new viscoelastic benchmark flow: Stationary bifurcation in a cross-slot. *J. Non-Newt. Fluid Mech.*, 214:57–68 (2014).

Appendix: Weissenberg number influence on the stress singularity

In this appendix, we consider the influence of the Weissenberg number on the numerical results in the vicinity of the singularity for the Oldroyd-B model and Newtonian kinematics on the M2 mesh. The Weissenberg numbers adopted for the investigations on the two benchmark problems (contraction and stick-slip) are $Wi = 1, 2, 5, 10$. For the contraction flow, Fig. 24 confirms that the asymptotic behaviours do not change with increasing Weissenberg number. The Weissenberg number does influence the coefficients of the leading asymptotic behaviours, which in the log-log plots manifests as differing vertical intercepts of the asymptotic lines. This is evident for both Cartesian and natural stress variables, with 24(b) showing that λ NS variable is the most sensitive. For the stick-slip problem, the effect of Wi variation is presented in Fig. 25. Numerical results for the extra-stress tensor and for natural stress variables, are presented respectively in Fig. 25 for $Wi = 1, 2, 5, 10$. Again, the leading order asymptotic behaviors of the variables in the vicinity of the singularity are independent of the selected Weissenberg numbers.

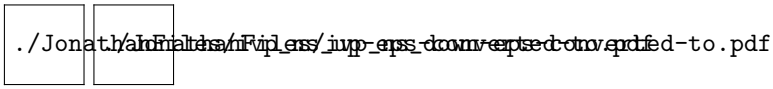

(a) (b)

Figure 1: Numerical results for the upstream and downstream boundary layer equations in the benchmark case of $\alpha = 270^o$. (a) illustrates convergence of the upstream solution to the far-field constants $C_1^* \approx 1.04716, C_2^* \approx -1.28566, C_3^* \approx 4.08804$, using the scaled variables $\ell/\xi^{2n_1+2}, m/\xi^{2n_2}, n/\xi^{2n_3-2}$. (b) illustrates convergence of the downstream solution to the wall condition (3.34).

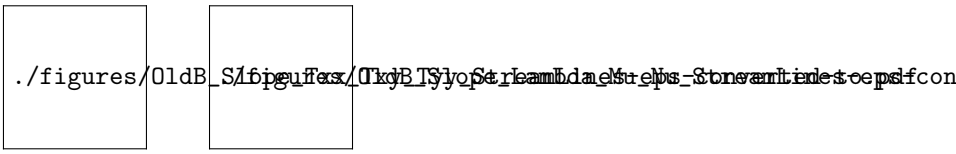

(a) CSF (b) NSF

Figure 2: Verification of the singularity behaviour for the (a) CSF and (b) NSF variables.

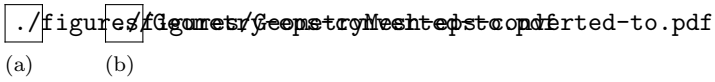

(a) (b)

Figure 3: Geometry of the $4:1$ contraction flow (a) and non-uniform mesh details (b).

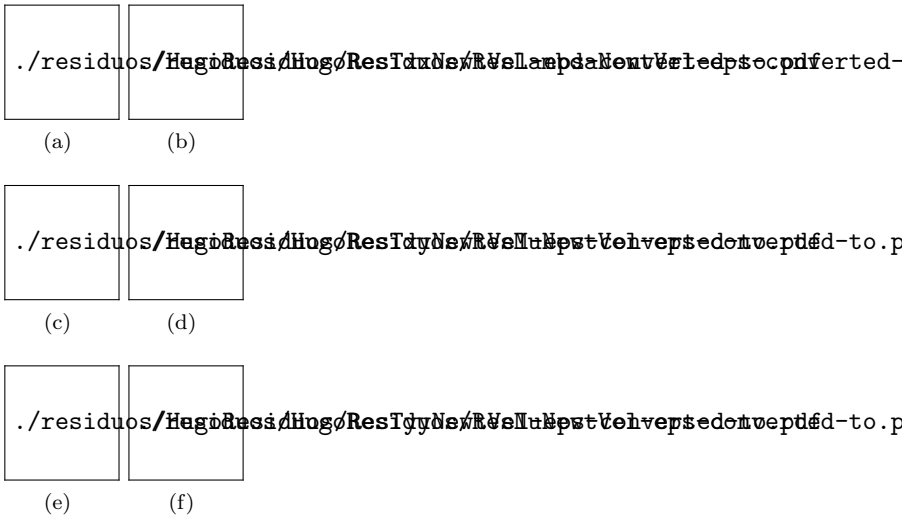

(a) (b) (c) (d) (e) (f)

Figure 4: Time variation of the CSF (left) and NSF (right) local residuals near to the singularity.

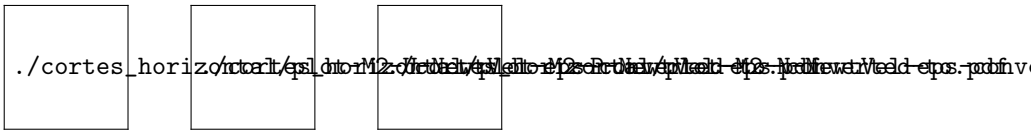

(a) (b) (c)

Figure 5: Horizontal profiles ($y = 0$) of u, p and $T_{22}^P - T_{11}^P$ at the steady-state for CSF and NSF considering the Newtonian velocity field.

Figure 6: Visualization of the colour map for the flow classification parameter ft with the Newtonian velocity field.

Figure 7: Zoom for the colour map visualization around the re-entrant corner with the Newtonian velocity field.

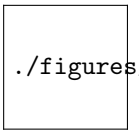

Figure 8: Illustration of the selected angles for studying the asymptotic behaviour near the singularity.

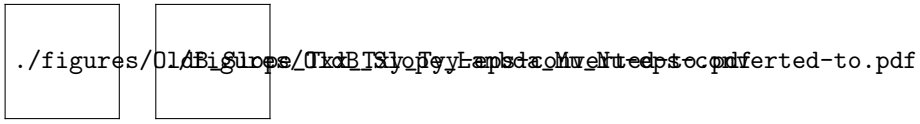

(a) $\theta = \frac{\pi}{2}$

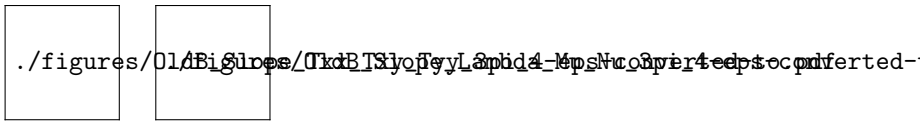

(b) $\theta = \frac{3\pi}{4}$

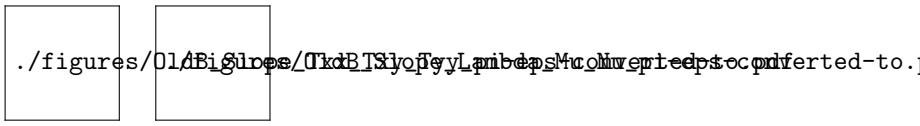

(c) $\theta = \pi$

Figure 9: Asymptotic variation near the singularity of $T_{11}^P, T_{12}^P, T_{22}^P$, λ, μ and ν along three different lines.

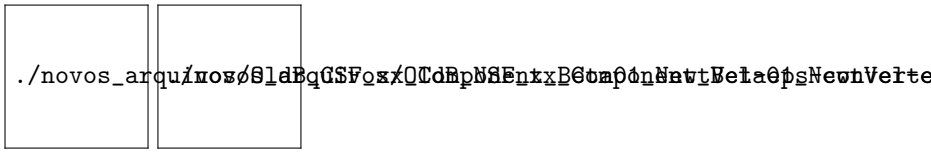

(a) CSF, ij = 11 (b) NSF, ij = 11

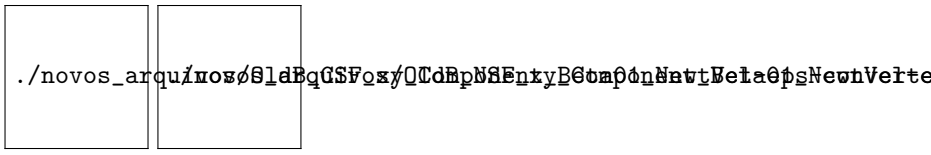

(c) CSF, ij = 12 (d) NSF, ij = 12

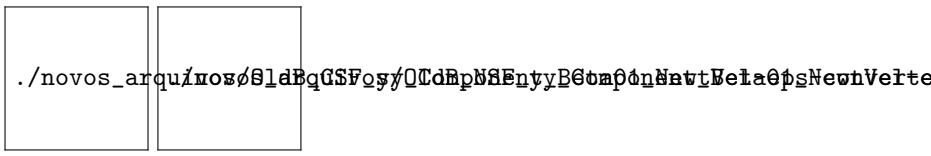

(e) CSF, ij = 22 (f) NSF, ij = 22

Figure 10: Dominance of the groups of terms for components 11, 12 and 22 within the Cartesian constitutive equation in a Newtonian velocity field: first column for CSF and second column for NSF.

Figure 11: Time variation of the CSF and NSF local residuals near to the singularity using the viscoelastic velocity field.

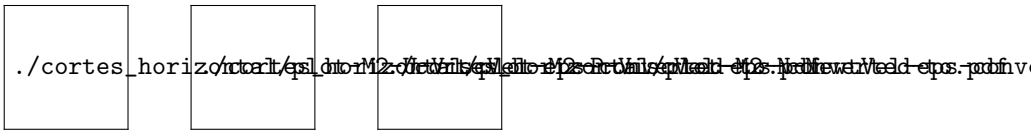

(a) (b) (c)

Figure 12: Horizontal profiles ($y = 0$) of u, p and $T_{22}^P - T_{11}^P$ at the steady-state for CSF and NSF considering the true viscoelastic velocity fields. For the viscoelastic velocity field, it was considered the hybrid version of the NSF [37], denoted as Hyb. NSF.

(a) (b)
CSF Hyb.

Figure 13: Visualization of the colour map for the flow classification parameter ft: a) CSF and b) NSF with the viscoelastic velocity field.

Figure 14: Zoom for the colour map visualization around the re-entrant corner: a) CSF and b) NSF with the viscoelastic velocity field.

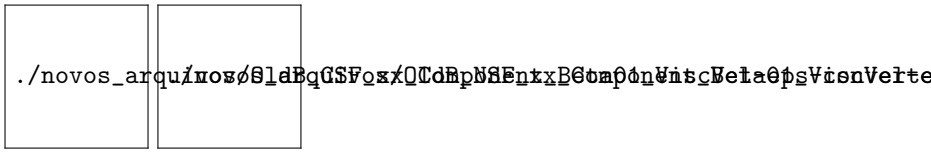

(a) CSF, ij = 11

(b) NSF, ij = 11

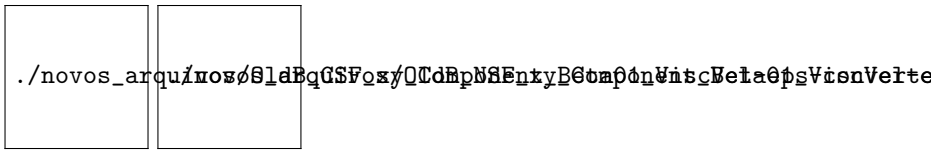

(c) CSF, ij = 12

(d) NSF, ij = 12

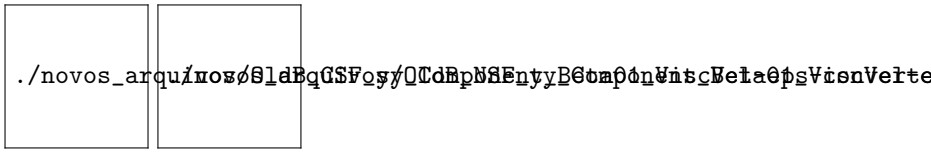

(e) CSF, ij = 22

(f) NSF, ij = 22

Figure 15: Dominance of the groups of terms for components 11, 12 and 22 within the Cartesian constitutive equation using the viscoelastic velocity field: first column for CSF and second column for NSF.

Figure 16: Stick-slip geometry.

Figure 17: Illustration of the selected angles for studying the asymptotic behaviour near the stick-slip transition point.

(a) $\theta = \frac{\pi}{4}$

(b) $\theta = \frac{\pi}{2}$

(c) $\theta = \frac{3\pi}{4}$

Figure 18: Asymptotic variation near the stick-slip transition point of T_{11}^P, T_{12}^P, T_{22}^P (left column) and λ, μ, ν (right column) along: (a) $\theta = \pi/4$, (b) $\theta = \pi/2$ and (c) $\theta = 3\pi/4$.

Figure 19: Horizontal profile of T_{11}^p along the line $y = 1$ for the Oldroyd-B, PTT and Giesekus models.

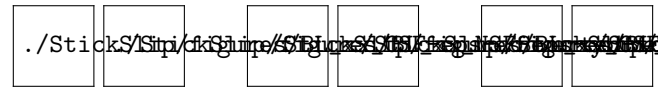

(a) $ij = 11$ (b) $ij = 11$ (c) $ij = 12$ (d) $ij = 12$ (e) $ij = 22$ (f) $ij = 22$

Figure 20: Dominance of the groups of terms (4.44) for components $11, 12$ and 22 within the Cartesian constitutive equation in a Newtonian velocity field: first column for CSF and second column for NSF.

(b)

(c)

(d)

(e)

(f)

Figure 21: Variation along the horizontal centreline ($y = 0$) for $De = 0.3$ and $De = 0.36$ considering meshes M1 and M2: components of the extra-stress tensor for CSF (first column) and NS variables (second column).

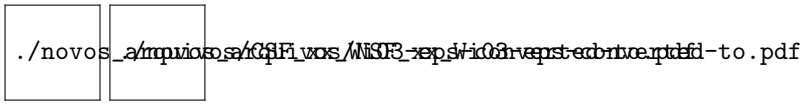

(a) CSF, $ij = 11$ (b) NSF, $ij = 11$

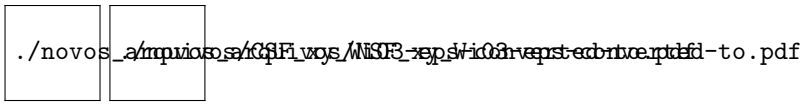

(c) CSF, $ij = 12$ (d) NSF, $ij = 12$

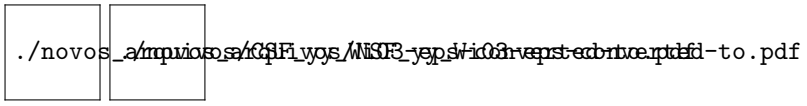

(e) CSF, $ij = 22$ (f) NSF, $ij = 22$

Figure 22: Dominance of the groups of terms for components 11, 12 and 22 within the Cartesian constitutive equation using $De = 0.3$: first column for CSF and second column for NSF.

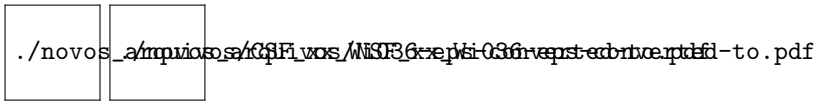

(a) CSF, $ij = 11$ (b) NSF, $ij = 11$

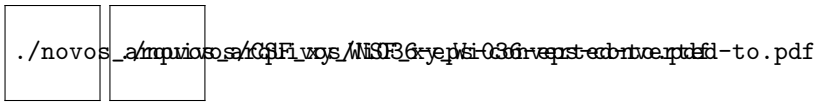

(c) CSF, $ij = 12$ (d) NSF, $ij = 12$

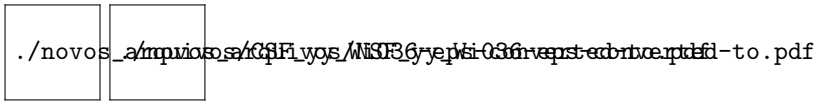

(e) CSF, $ij = 22$ (f) NSF, $ij = 22$

Figure 23: Dominance of the groups of terms for components 11, 12 and 22 within the Cartesian constitutive equation using $De = 0.36$: first column for CSF and second column for NSF.

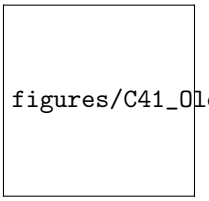

(a)

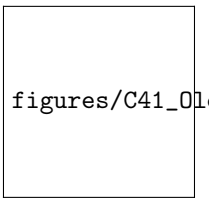

(b)

Figure 24: Verification of the singularity for the contraction flow for different values of $Wi = 1, 2, 5, 10$: (a) CSF and (b) NSF.

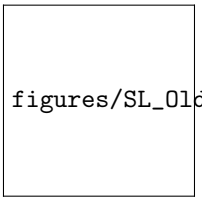

(a)

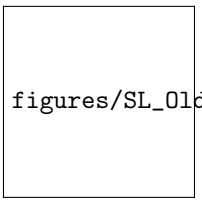

(b)

Figure 25: Verification of the singularity for the stick-slip flow for different values of $Wi = 1, 2, 5, 10$: (a) CSF and (b) NSF.

Table 1: Details of the non-uniform meshes.

Mesh	Space-step	Numbers of cells	Number of cells in the x and y directions
M1 (non-uniform)	$\frac{\delta x_{min}}{L} = \frac{\delta y_{min}}{L} = 0.008$	32300	190×260
M2 (non-uniform)	$\frac{\delta x_{min}}{L} = \frac{\delta y_{min}}{L} = 0.004$	48400	220×340

Table 2: Details of the non-uniform meshes.

Mesh	Space-step	Numbers of cells	Number of cells in the x and y directions
M1 (non-uniform)	$\frac{\delta x_{min}}{L} = \frac{\delta y_{min}}{L} = 0.005$	18000	180×100
M2 (non-uniform)	$\frac{\delta x_{min}}{L} = \frac{\delta y_{min}}{L} = 0.0005$	56000	280×200